formation in symptomatic carotid stenosis. J Vasc Surg 1997;26: 585-94.
19. Lozano P, Gomez FT, Julia J, M-Rimbau E, Garcia F. Recurrent embolism caused by floating thrombus in the thoracic aorta. Ann Vasc Surg 1998;12:609-11.
20. Mochizuki S, Takayama S, Nishiyama T, Kakizawa H, Shikaura K, Sakamoto M, et al. Two cases of protruding atherosclerotic plaque with mobile projections in the aortic arch. Intern Med 1993;32:777-80.
21. de Korte CL, Pasterkamp G, van der Steen AF, Woutman HA, Bom N. Characterization of plaque components with intravascular ultrasound elastography in human femoral and coronary arteries in vitro. Circulation 2000;102:617-23.
22. de Korte CL, Sierevogel MJ, Mastik F, Strijder C, Schaar JA, Velema E, et al. Identification of atherosclerotic plaque components with intravascular ultrasound elastography in vivo: a Yucatan pig study. Circulation 2002;105:1627-30.
23. Falk E. Stable versus unstable atherosclerosis: clinical aspects. Am Heart J 1999;138:S421-5.
24. Shah PK. Mechanisms of plaque vulnerability and rupture. J Am Coll Cardiol 2003;41:15S-22S.
25. Nighoghossian N, Derex L, Douek P. The vulnerable carotid artery plaque: current imaging methods and new perspectives. Stroke 2005; 36:2764-72.
26. Golledge J, Greenhalgh RM, Davies AH. The symptomatic carotid plaque. Stroke 2000;31:774-81.
27. Gutstein DE, Fuster V. Pathophysiology and clinical significance of atherosclerotic plaque rupture. Cardiovasc Res 1999;41:323-33.
28. Davies MJ, Richardson PD, Woolf N, Katz DR, Mann J. Risk of thrombosis in human atherosclerotic plaques: role of extracellular lipid, macrophage, and smooth muscle cell content. Br Heart J 1993;69: 377-81.
29. Felton CV, Crook D, Davies MJ, Oliver MF. Relation of plaque lipid composition and morphology to the stability of human aortic plaques. Arterioscler Thromb Vasc Biol 1997;17:1337-45.
30. Cappendijk VC, Kessels AG, Heeneman S, Cleutjens KB, Schurink GW, Welten RJ, et al. Comparison of lipid-rich necrotic core size in symptomatic and asymptomatic carotid atherosclerotic plaque: initial results. J Magn Reson Img 2008;27:1356-61.
31. Redgrave JN, Lovett JK, Gallagher PJ, Rothwell PM. Histological assessment of 526 symptomatic carotid plaques in relation to the nature and timing of ischemic symptoms: the Oxford plaque study. Circulation 2006;113:2320-8.
32. Russell DA, Wijeyaratne SM, Gough MJ. Changes in carotid plaque echomorphology with time since a neurologic event. J Vasc Surg 2007;45:367-72.
33. Spagnoli LG, Mauriello A, Sangiorgi G, Fratoni S, Bonanno E, Schwartz RS, et al. Extracranial thrombotically active carotid plaque as a risk factor for ischemic stroke. JAMA 2004;292:1845-52.

Submitted Aug 25, 2010; accepted Oct 18, 2010.

Additional material for this article may be found online at www.jvascsurg.org.

Evaluation of a Brain Imaging System with Combined Parallel Hole and Pinhole Collimation

Qiu Huang, Tsutomu Zeniya, Yoshiyuki Hirano, Hiroyuki Kudo, Hidehiro Iida, and Grant T. Gullberg

Abstract–This work evaluates the brain imaging system designed by the Department of Investigative Radiology at the National Cardiovascular Research Center- Research Institute in Osaka, Japan. As presented at the IEEE Nuclear Science Symposium and Medical Imaging Conference at Knoxville, TN in 2010, the high resolution single photon emission computed tomography (SPECT) imager was developed for obtaining high resolution brain scans for various imaging diagnostic applications. The system was mounted with one large field of view detector imaging the whole brain and multiple smaller field of view high resolution detectors imaging small regions of the brain. The large field of view detector provides images without truncation that localize areas of particular diagnostic interest and provide support information for the reconstruction of high resolution regions of interest (ROIs) from high resolution truncated projections obtained with the small field of view detectors. At the IEEE conference, the authors suggested a geometry which achieved high resolution reconstruction of the brain with a small pinhole aperture. The work presented in this paper simulates the camera with larger pinholes and shows that the camera has accurate quantitation and fine resolution for the interior reconstruction problem.

I. INTRODUCTION

SPECT plays an active role in brain imaging. For example, in clinical evaluation for diagnosing brain autoregulatory abnormalities, cerebral blood flow (CBF) and cerebral vascular reactivity (CVR) is quantified in a single session using a split dose administration of ^{123}I-iodo-amphetamine (IMP); one at rest and one during Diamox challenge. In addition, to evaluate neuronal damage due to ischemia and to provide prognostic value for surgical outcomes, Iodine-123-iomazenil (Iomazenil) is used to image the binding to benzodiazepine receptors prior to carotid endoarterectomy. To better quantify the brain function, the Department of Investigative Radiology at the National Cardiovascular Research Center - Research Institute in Osaka, Japan is designing a high resolution single photon emission computed tomography (SPECT) imager as shown in Fig. 1 for obtaining high resolution brain images. The camera consists of one large field of view detector imaging the whole brain and multiple smaller field of view high resolution detectors imaging small regions of the brain. The observed intrinsic spatial resolution of the large FOV detector in the x and y-direction are 3.5 mm and 3.1 mm, respectively. The intrinsic spatial resolution of the small FOV detector in the x and y-direction and the energy resolution are 2.3 mm, 2.4 mm, and 6.1 %, respectively [1].

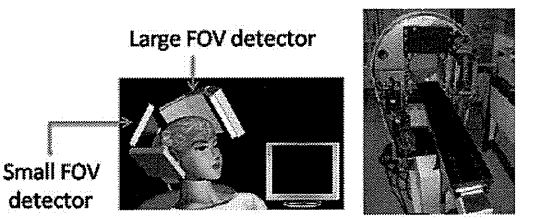

Figure 1. Camera with large field of view detector for imaging whole brain and smaller field of view detectors for imaging ROIs (left), and the prototype system (right).

The large field of view detector provides images without truncation that localize areas of particular diagnostic interest and provides support information for the reconstruction of high resolution regions of interest (ROIs) from high resolution truncated projections obtained with the small field of view detectors. The work presented in this paper provides simulations which show that the camera improves the quantitation for the interior reconstruction problem with a few multiple pinhole collimated detectors.

The pinhole collimator is able to achieve higher geometric resolution than a parallel-hole collimator. In addition, at a small object-to-detector distance, sensitivity of pinholes can be higher than that of the parallel-hole collimator [2]. However, the advantage is guaranteed at the expense of a smaller field of view, which results in truncated projections. The reconstruction of these projections involves determining the solution to the interior problem in local tomography. The interior problem in medical imaging refers to the

Manuscript received November 21, 2010. This work was supported by NIH under Grant No.R01EB00121, by the Director, Office of Science, Office of Biological and Environmental Research of the US Department of Energy under contract DE-AC02-05CH11231, by the Grant for Translational Research from the Ministry of Health, Labour and Welfare (MHLW), Japan, and by the Specialized Research Fund for the Doctoral Program of Higher Education (SRFDP), China, Grant No. 20100073120003.

Q. Huang is with the Shanghai Jiao Tong University, Shanghai, China (e-mail: huangjone@yahoo.com).

T. Zeniya, Y. Hirano and H. Iida are with the National Cardiovascular Center Research Institute, Suita, Osaka, Japan.

H. Kudo is with University of Tsukuba, Tsukuba, Japan.

G. T. Gullberg is with the Lawrence Berkeley National Laboratory, Berkeley, CA USA.

situation where the region-of-interest (ROI) is totally contained within the object. For instance, in SPECT, the interior problem happens when the projections passing through the region outside the ROI are truncated due to a small field-of-view detector or a short detector-to-object distance in the case of converging collimation. The interior problem has been studied for some time [3]. Recently, it was proven that the solution is unique and stable in computed tomography (CT) if a small region in the ROI is known *a priori* [4-9]. In this paper, the SPECT interior reconstruction problem is solved using an iterative algorithm as presented in [10].

To further increase the sensitivity of the system, the small FOV detector is mounted with multiple pinhole collimators. The pinhole apertures are chosen to be 2mm instead of 0.5mm in the previous work [10]. Stationary small FOV detectors are simulated to acquire data assuming the region of interest is at the center of the brain or at the posterior region of the brain.

The paper is organized as follows: Section II shows the method we used to simulate the combined parallel-hole and pinhole collimated imager and the algorithm to reconstruct the pinhole data. The result of a numerical simulation is presented in Section III where comparisons are made to illustrate the resolution and quantification of the camera. Then the conclusion is given in Section IV.

II. METHODS

We performed a simulation study using the digital XCAT brain phantom [11]. The phantom was stored in a 3-dimensional volume with each voxel being $(2mm)^3$. One slice of the phantom is shown in Fig. 2.

The large field of view parallel-hole collimated detector was simulated to revolve around the brain and acquire data every 5 degrees over half a circle. The detector bin was 0.28 cm along the transversal direction and 0.2 cm along the axial direction. Poisson noise was manually added to the data to give a noise level such that the total counts of each slice summed to 10^7. The filtered backprojection algorithm was applied to the simulated projection data to reconstruct a volumetric image. Fig. 3 gives an example of one slice of the reconstructed low resolution parallel data. The image was interpolated and smoothed and was later used as the initial image and as prior information in the reconstruction of the pinhole data. A mask image was also generated according to the reconstructed image from data acquired with large FOV parallel-hole collimated detectors, which was later used in the iterative reconstruction of data for the small FOV pinhole collimated detectors.

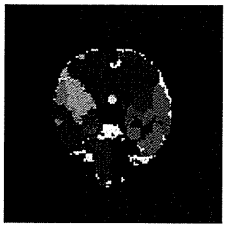

Fig. 2. The original XCAT phantom.

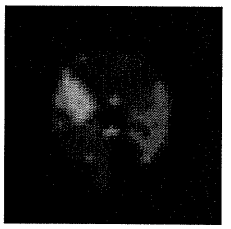

Fig. 3. The reconstructed image from parallel-hole projection data.

The pinhole collimator is shown in Fig. 4. It had a circular aperture with a radius of 2 mm and a knife edge with an opening angle of $\pi/3$.

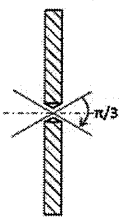

Fig. 4. The pinhole collimator. The pinhole is a circular aperture with a radius of 2mm and a knife edge with an opening angle of $\pi/3$.

In each small FOV detector, 3×3 pinholes were attached all focusing to common point, which could be the center of rotation though the detectors are stationary during data acquisitions. The view of the pinhole plane is shown in Fig. 5(a). Each pinhole is separated from the other by 5.5 mm both in the horizontal and vertical directions. The side view in Fig. 5(b) shows the geometry simulated in this work, which gives a magnification factor of 1.

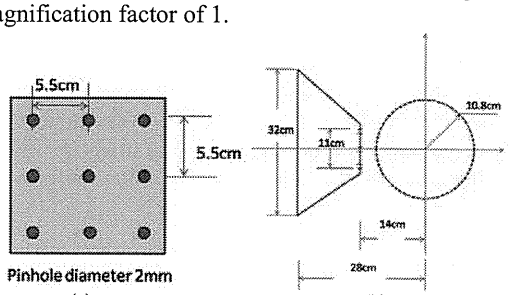

Fig. 5. Side view and top view of the multiple pinhole collimator. The plane with 3×3 pinholes (a), The side view of one detector head with the multiple pinhole collimation.

The small FOV detectors used a 2×2 H8500 PMT block for each pinhole. The 10×10 cm^2 blocks were connected with a 1cm septa in between to avoid overlap between projections through adjacent pinholes. The detector plane is illustrated in Fig. 6. The 2D detector plane had an area of 32×32 cm^2.

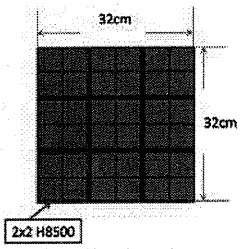

Fig. 6. The detector plane for a 3×3 pinhole collimator. Each pinhole is mounted with a 2×2 H8500 PMT block.

Four small FOV detectors were then localized close to the object as shown in Fig. 7. The FOV is then a sphere with a radius of 5mm. In other words, the projections were truncated. One view is shown in Fig. 8. In the figure, the detector bin is 2 mm.

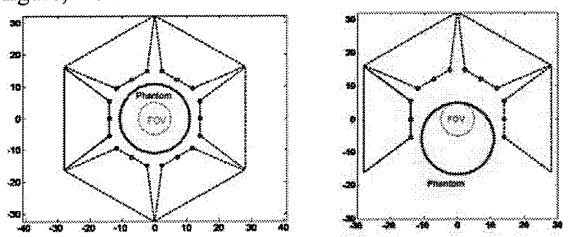

Fig. 7. The two geometries simulated in this work.

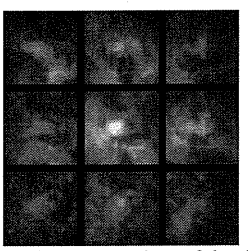

Fig. 8. The projection at one view of the 6 views for the geometry on the left shown in Fig. 7.

The reconstruction algorithm was developed to maximize *a posteriori* probability of the image given the simulated projections. Details could be found in [10].

III. Results

There are two geometries simulated in this work for the small FOV detectors: first one with 6 detector heads and the second with 4 detector heads, as shown in Fig. 7. In addition to the XCAT phantom, a point source phantom was also used to evaluate the system resolution.

The study with the XCAT phantom is shown in Fig. 9. The reconstructed images are from the geometry with 6 and 4 projection views, respectively. Profiles are plotted in Fig. 10 to show that the two geometries both improve the details in the reconstructed images over that obtained with the parallel-hole collimated detector. For the geometry with 6 views, the FOV is located at the center of the brain. While for the geometry with 4 views, the FOV is located at the posterior region of the brain. Both FOVs were reconstructed with higher resolution compared to the reconstruction shown in Fig. 3. Another comparison was performed with the point source phantom.

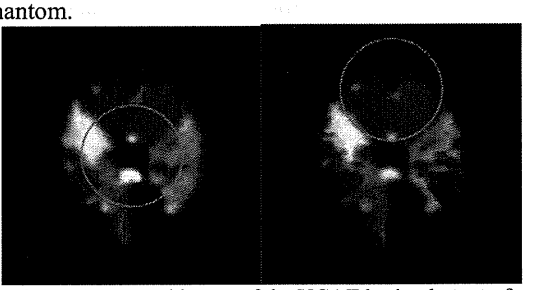

Fig. 9. Reconstructed image of the XCAT brain phantom from pinhole data for the interior problem and for limited angular sampling. MAP estimate with regularization is applied, for the geometry with 6 views (left) and for the geometry with 4 views (right). The circle on the image indicates the FOV.

In the simulation, the pinhole data were acquired with truncation, resulting in reconstructing an interior problem. Efforts should be made to correct for the effect of this problem. In this work, we used the low resolution image obtained by the large field of view detector first as the initial estimate in the iterative reconstruction of the pinhole data. Also, the low resolution image provided a priori information and a mask for the reconstruction of the interior problem. The prior information was used to calculate the L2 norm distance from the reconstructed image to compose the penalty term in addition to the total variation regularization. The image quality within the FOV, which was the central part of the brain for the geometry with 6 views and the posterior region of the brain for the geometry with 4 views, was improved.

The vertical and horizontal profiles crossing the FOV are shown in Fig. 10. From the profiles we see that the details of the image are more distinct by reconstructing both parallel-hole projection data and pinhole projection data; for instance, the details indicated by the arrows in Fig. 10.

The study with point source phantom is shown in Fig. 11 for the geometry with 6 views. In the reconstruction, no prior information was used, however the total variation regularization was used in the iteration. The image shows that the resolution of the system is fairly good. Although with the truncation problem, the quantification is degraded.

Profiles for the three points labeled in Fig. 11 with the three arrows are drawn in Fig. 12. The dash lines (red) indicate the original phantom, and the solid lines (blue) are for the reconstructed images. The profiles imply high resolution for the system, however, with degradation of

quantitation for points off the FOV, for example, points 1 and 3.

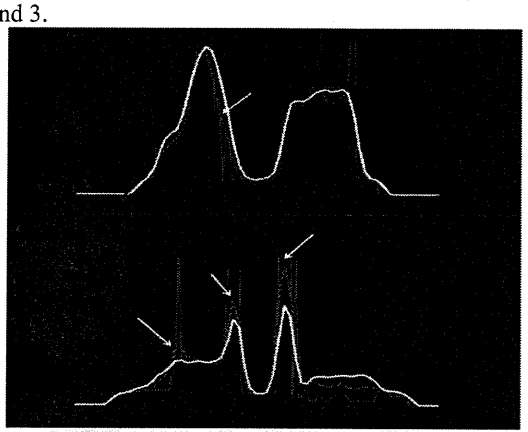

(a)

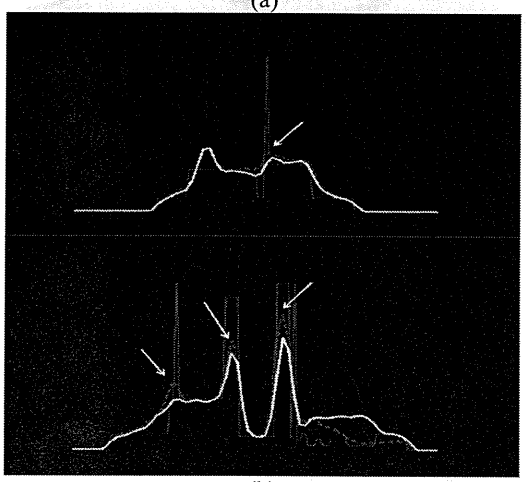

(b)

Fig. 10. Horizontal and vertical profiles crossing the center of the FOV for the geometry with 6 views (a) and for the geometry with 4 views (b). The purple solid line (thin) indicates the original phantom. The yellow dot-dash line is for the reconstructed image (Fig. 3.) from parallel-hole collimated data. While the red solid line (thick) is for the reconstructed image in Fig. 9.

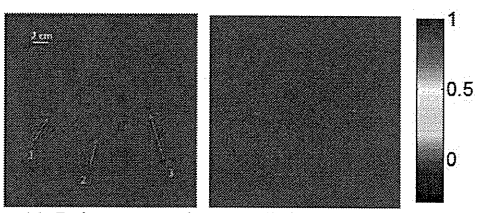

Fig. 11. Point source phantom (left) and the reconstructed image of the point source phantom for the geometry with 6 views (right).

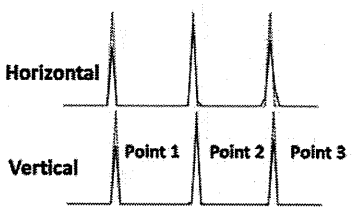

Fig. 11. The horizontal and vertical profiles for lines passing through the three points indicated in Fig. 11.

IV. Conclusion

The combination of a large field of view parallel-hole collimated detector and smaller field of view high resolution pinhole detectors improves the quantitation in simulated brain imaging. It makes use of the high sensitivity of the pinhole collimator while compensates for the degradation in the reconstructed image due to the interior reconstruction problem caused by the small field of view of the pinhole collimator. This work will be verified through phantom imaging studies.

References

[1] Y. Hirano, T. Zeniya, and H. Iida, "Development of a high resolution and quantitative SPECT for the human brain," *IEEE Nuclear Science Symposium and Medical Imaging Conference*, Knoxville, TN, 2010.

[2] R. J. Jaszczak, J. Li, H. Wang, M. R. Zalutsky, and R. E. Coleman, "Pinhole collimation for ultra-high-resolution, small-field-of-view SPECT," *Phys. Med. Biol.*, vol. 39, pp. 425-437, 1994.

[3] F. Natterer, *The Mathematics of Computerized Tomography* (SIAM), 1986.

[4] G. Wang, Y. Ye and H. Yu, "General VOI/ROI reconstruction methods and systems using a truncated Hilbert transform," Patent disclosure submitted to Virginia Tech. Intellectual Properties on May 15 2007.

[5] Y. Ye, H. Yu, and G. Wang, "Exact interior reconstruction with cone-beam CT," *Int. J. Biomed. Imaging*, Article ID. 10693, 2007.

[6] Y. Ye, H. Yu, Y. We and G. Wang, "A general local reconstruction approach based on a truncated Hilbert transform," *Int. J. Biomed. Imaging*, Article ID. 63634, 2007.

[7] Y. Ye, H. Yu, and G. Wang, "Exact interior reconstruction from truncated limited-angle projection data," *Int. J. Biomed. Imaging*, Article ID. 427987, 2008.

[8] M. Courdurier, F. Noo, M. Defrise and H. Kudo, "Solving the interior problem of computed tomography using a priori knowledge," *Inverse Problems*, vol. 24, pp. 065001, 2008.

[9] H. Kudo, M. Courdurier, F. Noo, and M. Defrise, "Tiny a proiri knowledge solves the interior problem in computed tomography," *Phys. Med. Bio.*, vol. 53, pp. 2207-2231, 2008.

[10] Q. Huang, T. Zeniya, H. Kudo, H. Iida, and G. T. Gullberg, "High resolution brain imaging with combined parallel hole and pinhole collimation," *IEEE Nuclear Science Symposium and Medical Imaging Conference*, Knoxville, TN, 2010.

[11] W. P. Segars and B. M. W. Tsui, "MCAT to XCAT: the evaluation of 4-D computerized phantoms for imaging research," *Proceedings of the IEEE*, vol. 97, No. 12, 2009.

Row-Action Image Reconstruction Algorithm Using ℓ_p-Norm Distance to a Reference Image

Essam A. Rashed, *Member, IEEE,* and Hiroyuki Kudo, *Member, IEEE*

***Abstract*—This work investigates the problem of image reconstruction from small number of projection views in x-ray computed tomography (CT) imaging. The number of acquired projection views has a large influence on accuracy and stability of the image reconstruction problem. However, measuring the projection data over small number of views leads to a patient dose reduction and/or minimization of imaging time which become a principal target in many clinical applications. The presented work aims to develop a row-action type reconstruction algorithm that include *a priori* known information extracted from a reference image. The proposed method is based on the fact that, in many CT imaging applications, some physical and anatomical structures and the corresponding attenuation information of the scanned object can be *a priori* known. The main idea is to include a distance function consisting of ℓ_p norm of the reconstructed image into the cost function for image reconstruction. The constrained minimization problem is then transferred to the corresponding non-constrained maximization dual problem using Lagrangian duality. Experimental results indicate that the proposed reconstruction algorithms can effectively reduce the streak artifacts when a simple reference image is used.**

I. Introduction

In this paper, we investigate the problem of image reconstruction from small number of projection views in x-ray computed tomography (CT) imaging. The number of acquired projection views has a large influence on accuracy and stability of the image reconstruction problem. However, in many imaging applications, the available projection data are limited to only a small number of views less than theoretically required by Shannon-Nyquist sampling theorem [1]. Moreover, measuring the projection data over small number of views, as shown in Fig. 1, leads to a patient dose reduction and/or minimization of imaging time which become a principal target in many clinical applications. It is known that image reconstructed from such limited data suffers from streak/aliasing artifacts that degrade image quality. In literature, several approaches have been proposed to overcome this problem for different clinical applications (e.g. [2]–[5]).

The presented work aims to develop a row-action type reconstruction algorithm that include *a priori* known information extracted from a reference image. The main idea is to include a distance function consisting of ℓ_p norm of the reconstructed image into the cost function for image reconstruction. The constrained minimization problem is then transferred to the corresponding non-constrained maximization dual problem using Lagrangian duality. As detailed later, using the concept of Lagrangian duality enable us to optimize the cost function using a simple gradient approach.

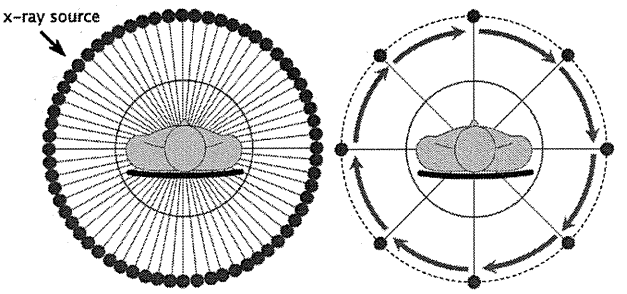

Fig. 1. CT imaging configurations. The positions of x-ray source for data acquisition for full scan (left) and limited views (right).

II. Imaging Model

A. Compressed sensing and image sparsity

The recently introduced theory of compressed sensing, becomes an important approach to solve the data limitation problems in tomographic imaging and several other signal processing applications [6], [7]. The main idea is based on the minimization of the cost function that include ℓ_1/ℓ_0 norm of a sparse representation of the target image. It is easy to observe the powerful of ℓ_1/ℓ_0 norm and similar functions in finding the sparse solution from several feasible ones. Hence, it is widely used to solve the under-determinant inverse problems. However, in many medical imaging applications, the target object is non-sparse and additional sparsification transformation such as image gradient or wavelet transform is employed.

In the presented approach, we assume that a reference image that represent normal and expected structures of the scanned object is *a priori* known. When the reference image becomes closer to the reconstructed image, the difference takes the form of sparse image. Let $\vec{x} = (x_1, \ldots, x_n)^\top$ denotes the image vector, we can represent the reconstructed image as the sum of two components. $\vec{x} = \vec{u} + \vec{v}$, where $\vec{u} = (u_1, \ldots, u_n)^\top$ represents the *reference image* and $\vec{v} = (v_1, \ldots, v_n)^\top$ is the *sparse image* which includes unknown regions (such as lesions, tumors, abnormalities,...,etc.) that cannot be expected in prior to the reconstruction. Medical imaging dedicated for

This work was partially supported by Grant-in-Aid from the Japan Society for the Promotion of Science (JSPS). Grant for foreign Post-doctoral fellows (ID No. P10052).

E.A.Rashed and H.Kudo are with the Department of Computer Science, Graduate School of Systems and Information Engineering, University of Tsukuba, Tsukuba 305-8573, Japan. E.A.Rashed is also with the Department of Mathematics, Faculty of Science, Suez Canal University, Ismailia 41522, Egypt (e-mail: essam@imagelab.cs.tsukuba.ac.jp).

978-1-4673-0119-0/11/$26.00 ©2011 IEEE

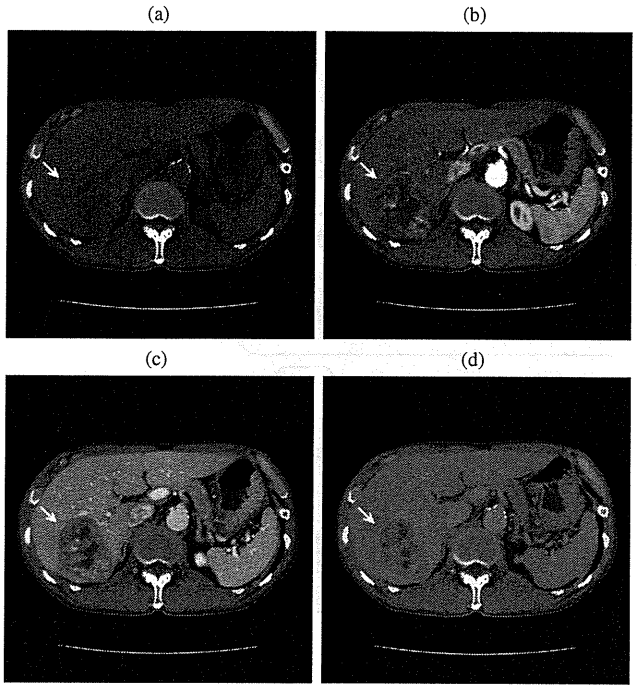

Fig. 2. A single slices of four-phase abdominal CT images of 65 years old patient with liver tumor. Image reconstructed from scan during (a) pre-contrast phase, (b) early phase, (c) portal phase and (d) late phase. Display window is [-130,260]HU.

diagnosis, in many cases, aims to investigate the existence of regions belong to $\vec{v}$ in the imaged object. As the contribution of components $\vec{v}$ to $\vec{x}$ is relatively small compared to that of $\vec{u}$, the image sparisty can be enforced by including the component $\vec{u}$ in the image reconstruction cost function.

B. Create a reference image

The *a priori* knowledge of a reference image can be computed in effective way in several x-ray CT applications. We will discuss a single example that describe how to compute a good reference image in clinical applications. We consider the four-phase abdominal CT imaging. In this imaging protocol, the patient is subject to be scanned four times in pre-contrast, early, portal and later phases. Example of images resulted from this clinical application are shown in Fig. 2. This imaging protocol is important for an effective diagnosis of liver tumors and other diseases in the abdominal region. However, it provides the patient with extremely high dose and uncomfortable long time scan. To reduce the patient dose and imaging time, we proposed the following low-dose protocol. First, we scan the patient with normal dose to obtain the image corresponding to the pre-contrast scan. This image is used to create a reference image to be included in the reconstruction of successive low-dose or small views scans corresponding to the early, portal and later phases. As the four scans are done within the same imaging session, we expect that a simple pre-processing calculations including calibration and image registration can be used to provide a high quality reference image for effective dose reduction in later scans. An illustration of the proposed modification in this imaging protocol is shown in Fig. 3 The fine details of the pre-processing step is not included here and is beyond the scope of this paper.

III. Proposed Method

A. Cost function and minimization strategy

The proposed reconstruction method is based on minimizing the following cost function:

$$\|\vec{x}-\vec{u}\|_p^p/p \text{ subject to } A\vec{x}=\vec{y}, \vec{x}\geq 0, \quad (1<p\leq 2). \quad (1)$$

where $\vec{y}=(y_1,\ldots,y_m)^\top$ is the measured projection data and $A=\{a_{ij}\}$ is the $m\times n$ matrix that model the x-ray CT system. As $m \ll n$, the number of feasible solutions of problem (1) is large. The ℓ_p norm distance between $\vec{x}$ and $\vec{u}$ aims to enforce image sparisty, considering that $\vec{u}$ is relatively close to $\vec{x}$. The optimization problem constraint represents a data fidelity term $A\vec{x}=\vec{y}$ to ensure the consistency between the reconstructed image $\vec{x}$ and the projection data $\vec{y}$. The motivations behind using ℓ_p norm with $(1<p\leq 2)$ instead of ℓ_1/ℓ_0 to solve this problem are: (1) unlike ℓ_1/ℓ_0 norm, the resulting problem is convex, (2) it is possible to maximize the corresponding dual problem with simple gradient methods and (3) when p is close to 1.0, it can achieve a similar performance to ℓ_1 norm in finding the sparse solution. In the results presented here, we have used $p=1.1$.

The cost function in Eq. (1) is optimized using the Lagrangian duality [8], [9]. Consider the following optimization problem with the linear equality constraint:

$$\text{minimize } F_{\vec{u}}(\vec{x}) \text{ subject to } A\vec{x}=\vec{y}, \quad (2)$$

$$F_{\vec{u}}(\vec{x})=\|\vec{x}-\vec{u}\|_p^p/p.$$

The Lagrange dual problem associated with the problem in Eq. (2) is donated as:

$$\text{maximize } D(\vec{\lambda}), \quad (3)$$

$$D(\vec{\lambda})=\inf_{\vec{x}\in\mathbf{dom}(F)}\mathcal{L}(\vec{x},\vec{u},\vec{\lambda}),$$

where $\vec{\lambda}=(\lambda_1,\ldots,\lambda_m)^\top$ is the vector of dual variables (or Lagrange multipliers) with optimal value given by $\vec{\lambda}^*$ and $\mathcal{L}(\vec{x},\vec{u},\vec{\lambda})$ is the Lagrangian function associated with Eq. (2) and is defined as:

$$\mathcal{L}(\vec{x},\vec{u},\vec{\lambda})=F_{\vec{u}}(\vec{x})-\lambda^\top(A\vec{x}-\vec{y}). \quad (4)$$

The conjugate function of $F_{\vec{u}}(\vec{x})$ is then defined as:

$$G_{\vec{u}}(\vec{y})=\sup_{\vec{x}\in\mathbf{dom}(F)}\left(\vec{y}\cdot\vec{x}-F_{\vec{u}}(\vec{x})\right), \quad (5)$$

with prime dual relation defined as $\vec{x}^*=\nabla G(A^\top\vec{\lambda}^*)$, where $\vec{x}^*$ is the minimum value for problem in Eq. (2).

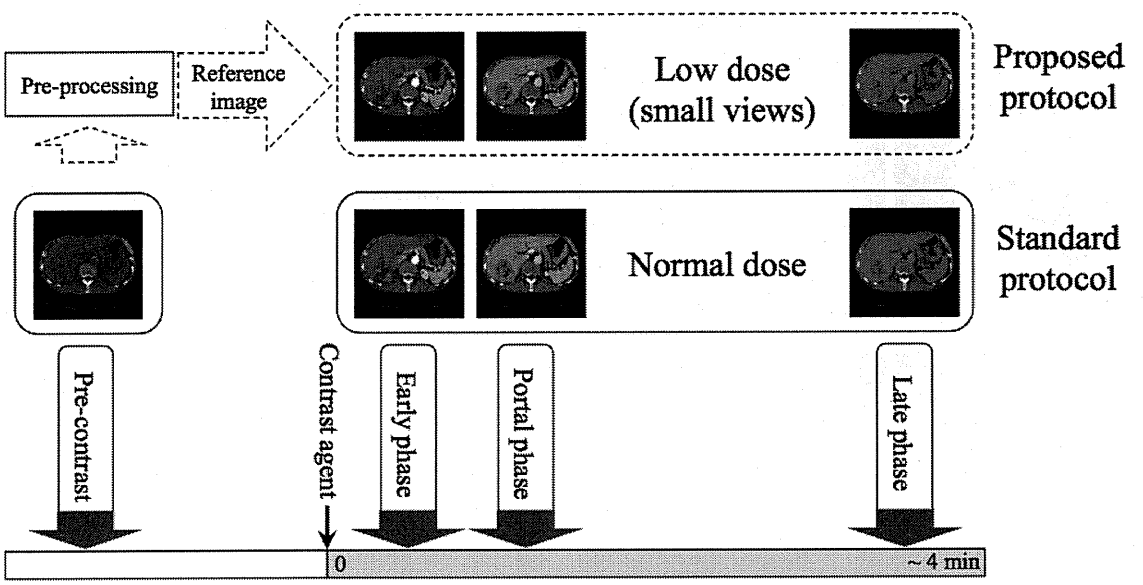

Fig. 3. Four-phase abdominal CT imaging protocol and the proposed modifications to reduce the patient dose.

B. Iterative reconstruction algorithm

The linear program in Eq. (1) can be rewritten as follows:

$$\text{minimize } \sum_{j=1}^{n} \frac{1}{p}|x_j - u_j|^p \text{ subject to } A\vec{x} = \vec{y}, \vec{x} \geq 0, \quad (6)$$

with corresponding dual problem defined as:

$$\text{maximize } D(\vec{\lambda}) = \vec{y}^{\top}\vec{\lambda} - G_{\vec{u}}(A^{\top}\vec{\lambda}), \quad (7)$$

where the conjugate function $G_{\vec{u}}$ is defined as:

$$G_{\vec{u}}(\vec{b}) = \sum_{j=1}^{n} g_{u_j}(b_j), \quad (8)$$

$$g_a(t) = \begin{cases} -\frac{1}{p}a^p & (t < -a^{p-1}) \\ \frac{1}{q}|t|^q + at & (t \geq -a^{p-1}) \end{cases}, \quad q = \frac{p}{p-1}.$$

The dual problem in Eq. (7) is solved using the coordinate ascent method to get the optimal value $\vec{\lambda}^*$, then $\vec{x}^*$ is computed using the following primal-dual relation:

$$x_j^* = g'_{u_j}(A^{\top}\vec{\lambda}^*|_j), \quad (9)$$

$$g'_a(t) = \begin{cases} 0 & (t < -a^{p-1}) \\ \text{sgn}(t)|t|^{q-1} + a & (t \geq -a^{p-1}) \end{cases}. \quad (10)$$

The iterative reconstruction algorithm is implemented as follows. First, we iteratively solve the maximization problem in Eq. (7) to obtain the dual solution $\vec{\lambda}^*$, Then, the primal-dual relation in Eq. (9) is used to find the corresponding solution of the original problem in Eq. (6). The proposed Raw-Action algorithm using Reference Image, which we called RARI, is summarized as follows:

Compute reference image $\vec{u} = (u_1, \ldots, u_n)$
Initialization $w^{(0)} = (0, \ldots, 0)$, $k \leftarrow 0$
repeat
  $\vec{w}^{(k,1)} = \vec{w}^{(k)}$
  for $i = 1 : m$ **do**
    $\vec{w}^{(k,i+1)} = \vec{w}^{(k,i)} + \beta\Delta_i(w_1^{(k,i)}, \ldots, w_n^{(k,i)})\vec{a_i}$
  end
  $\vec{w}^{(k+1)} = \vec{w}^{(k,m+1)}$
  $k \leftarrow k + 1$
until *stopping criterion*;
for $j = 1 : n$ **do**
  $x_j^* = g'_{u_j}(w_j^{(k+1)})$
end

where β is a relaxation parameter and the component Δ_i is the update for the coordinate ascent method used to solve problem in Eq. (7) and is defined as:

$$\Delta_i(w_1, \ldots, w_n) = \frac{y_i - \sum_{j=1}^{n} a_{ij} g'_{u_j}(w_j)}{\max(\Gamma, \sum_{l=1}^{n} a_{il}^2 h_{u_l}(w_l))}, \quad (11)$$

$$h_a(t) = \begin{cases} 0 & (t < -a^{p-1}) \\ \frac{1}{2}(q-2)a^{2-p} & (t = -a^{p-1}) \\ (q-2)|t|^{q-2} & (t > -a^{p-1}) \end{cases}.$$

where $h(.)$ is an approximation to the second derivative of $g_a(t)$ as it is undefined at $t = -a^{p-1}$ and Γ is an upper bound constant to avoid the vanishing of the denominator [9].

IV. Experimental Results

A. Simulation study

A simulation study was performed using a modified version of the Shepp-Logan phantom. The target of image recon-

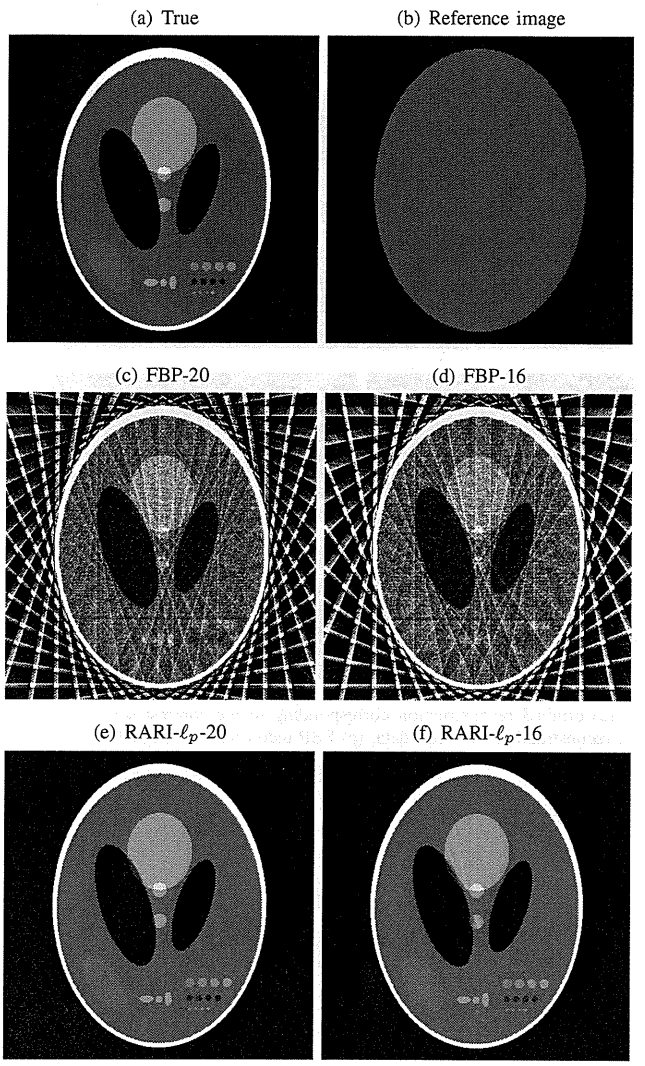

Fig. 4. Reconstruction results of the modified Shepp-Logan phantom in (a). Image reconstructed from 20 and 16 projection views using standard FBP in (c) and (d) and using RARI in (e) and (f), respectively. The reference image used for RARI method is in (b).

struction here is to reduce the image streak artifacts without losing the contrast of the insert spots. An object matrix of 512×512 pixels is projected over 512(bins) and 20/16 (views) over 180° with parallel-beam geometry. The reference image $\vec{u}$ is assumed to be a uniform image registered perfectly with the true object, as shown in Fig. 4(b). The simulation was performed through 500 iterations with Γ =256 and β =0.4 and 1.0 for m = 20 and 16, respectively. Reconstructed images from the proposed method and the conventional Filtered Backprojection (FBP) are shown in Fig. 4. It is clear from these simulated data that the proposed method can significantly suppress streak artifacts when the projection data is measured over small number of projection views (16 projections) by using a simple uniform reference image. However, it is worth noted that the high image sparsity which we can achieve in simulated data using digital phantoms is practically difficult to be available when we move to the case of real data.

B. Pseudo real data

The proposed method was applied to a pseudo real data for abdominal CT scans of two patients. As the original data is not available, we have used a previously reconstructed CT volumes from medical image database [10] and the projection data was created by a forward-projection of a single image slice. The original data were scanned using x-ray power of 120KeV and reconstructed in volumes with slice size of 512 × 512 pixels with $0.63mm$ pixel size. The image corresponding to the pre-contrast phase is used as a reference image to reconstruct the image corresponding to the portal-phase from small number of projection views. Image reconstruction from 100 projections was implemented with 10 iterations, Γ = 128, and β = 0.1. This experiment was repeated for data obtained from two patients. Results are compared with the original reconstruction from full data for a quality assessment. As shown in Fig. 5, image reconstructed from small number of projection views using FBP algorithm suffers from streak artifacts. However, when the information of the reference image is included into the reconstruction using RARI-ℓ_p algorithm, the image quality is enhanced and could be compared to original image reconstructed from full projection data.

V. Conclusion

We proposed a new row-action image reconstruction algorithm from small number of projection views. The main approach is based on minimizing the ℓ_p norm distance to *a priori* known reference image. The constrained minimization problem is converted to unconstrained maximization using Lagrangian duality. The resulting problem is much easier to solve with p = 1.1. The proposed algorithm has a large possibilities to be used in clinical application for the purpose of patient dose reduction. We have presented a modification to four-phase abdominal CT scan for significant reduction of ionization radiation. The results demonstrate that the proposed method is superior in preserving image quality even for small and low-contrast structures, when the projection data is highly under-sampled. Future work include a more sophisticated analysis for quantitative assessment of the proposed method. It is also interesting to investigate the possibilities to use the proposed method in solving other data limitation problems such as limited-angle problem.

References

[1] F. Natterer, *The Mathematics of Computerized Tomography*, Philadelphia, PA: Wiley, 1986.
[2] S. Siltanen, V. Kolehmainen, S. Järvenpää, J. P. Kaipio, P. Koistinen, M. Lassas, J. Pirttilä and E. Somersalo, "Statistical inversion for medical X-ray tomography with few radiographs: I. General theory," *Phys. Med. Biol.*, vol. 48, pp. 1437-1463, 2003.
[3] E. Y. Sidky, C.-M. Kao and X. Pan, "Accurate image reconstruction from few-views and limited-angle data in divergent-beam CT," *J. X-Ray Sci. Technol.*, vol. 14, pp. 119-139, 2006
[4] S. Leng, J. Tang, J. Zambelli, B. Nett, R. Tolakanahalli and G.-H. Chen, "High temporal resolution and streak-free four-dimensional cone-beam computed tomography," *Phys. Med. Biol.*, vol. 53, pp. 5653-5673, 2008.
[5] E. A. Rashed and H. Kudo, "Intensity-based Bayesian framework for image reconstruction from sparse projection data," *Med. Imag. Tech.*, vol. 27, pp. 243-251, 2009.
[6] D. L. Donoho, "Compressed sensing," *IEEE Trans. Inf. Theory*, vol. 52, pp. 1289-1306, 2006.

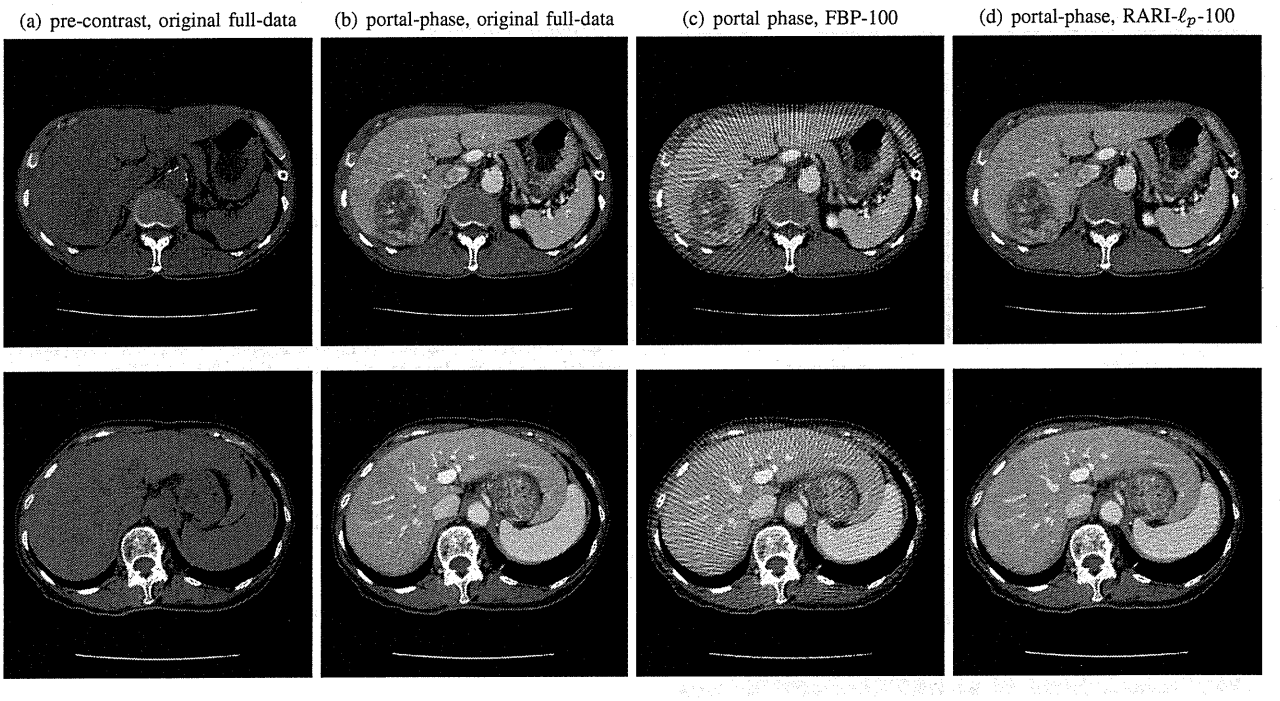

Fig. 5. Reconstruction of abdominal CT scan of two patients in separate rows. (a) original reconstruction corresponding to pre-contrast scan, used as a reference image, and reconstruction corresponding to portal phase using (b) original reconstruction from full data, (c) FBP reconstruction from 100 projection views, and (d) RARI-ℓ_p reconstruction from 100 projection views.

[7] E. J. Candès, J. Romberg and T. Tao, "Robust uncertainty principles: exact signal reconstruction from highly incomplete frequency information," *IEEE Trans. Inf. Theory*, vol. 52, pp. 489-509, 2006.
[8] D. P. Bertsekas, *Nonlinear Programming*. Massachusetts: Athena-Scientific, 1995.
[9] M. Li, H. Yang and H. Kudo, "An accurate iterative reconstruction algorithm for sparse objects: application to 3D blood-vessel reconstruction from limited number of projections," *Phys. Med. Biol.*, vol. 47, pp. 2599-2609, 2002.
[10] JAMIT medical image database (http://jamit.jp/cad-committe/caddbinfo)

Adaptive Thresholding for Robust Iterative Image Reconstruction from Limited Views Projection Data

Essam A. Rashed, *Member, IEEE,* Zhen Wang and Hiroyuki Kudo, *Member, IEEE*

***Abstract*—X-ray computed tomography (CT) is generally obtained through a reconstruction of object attenuation function from its projection data acquired through many angle views. However, in some cases the number of projection views is limited to only a small number that is theoretically not enough for stable reconstruction. The theory of compressed sensing (CS) introduce a new framework for solving this problem. In this paper, we present a simple iterative thresholding image reconstruction algorithm that include a minimization of cost function that include Log-likelihood and ℓ_1 norm distance to a reference image. The resulting thresholding function in the reconstruction algorithm is approximated with adaptive function that can preserve low-contrast regions from incorrect thresholding. Moreover, we present a simple approach to handle registration error between the reconstructed image and the reference. This approach is based on using dynamic reference image that generated from previous estimation of the reference image and the current image estimate. The proposed method proved to be robust in image reconstruction from small number of projection views through a simulation study.**

I. Introduction

Computed Tomography (CT) imaging is generally obtained through a reconstruction of object attenuation function from its projection data acquired through many angle views. The sampling rate and acquisition orbit of the scanner are important factors to determine the exactness of the image reconstruction problem. This work investigates the problem of image reconstruction from a small number of projection views. It is well-known that the reduction of data acquisition sampling rate in the angular domain appears in the reconstructed images as streak artifacts. However, it becomes important to investigate stable reconstruction from a small number of projections in many medical imaging and industrial applications. The recently emerged theory of compressed sensing (CS) provides a new framework for this problem [1], [2]. Several approaches were proposed to solve this problem based on the theory of CS (e.g. [3]–[5]).

We consider that a reference image of the scanned object is *a priori* known. The cost function for image reconstruction is designed to include the *a priori* known information. In this study, we extending our previous work in [5] with an adaptive soft-thresholding reconstruction algorithm from limited projection data. The thresholding function is approximated with a corresponding convex function. Moreover, a better distance function is identified using global pixel information to control prior uncertainty when reference image is used.

This work was partially supported by Grant-in-Aid from the Japan Society for the Promotion of Science (JSPS). Grant for foreign post-doctoral fellows (ID No. P10052).

E.A.Rashed, Z.Wang and H.Kudo are with the Department of Computer Science, Graduate School of Systems and Information Engineering, University of Tsukuba, Tsukuba 305-8573, Japan. E.A.Rashed is also with the Department of Mathematics, Faculty of Science, Suez Canal University, Ismailia 41522, Egypt (e-mail: essam@imagelab.cs.tsukuba.ac.jp).

II. Proposed Method

A. Image reconstruction framework

We consider the following imaging model:

$$y_i \approx \text{Poisson}\ [b_i \exp(-\langle \vec{a_i}, \vec{x} \rangle)] \tag{1}$$

where $\vec{x} = (x_1, \ldots, x_n)^\top$ is the image vector, $\vec{y} = (y_1, \ldots, y_m)^\top$ be the measured counts, $\vec{b} = (b_1, \ldots, b_m)$ is the blank scan, $A = \{a_{ij}\}$ is the $m \times n$ system matrix and $\langle ., . \rangle$ is the regular inner product. The cost function for image reconstruction is defined as:

$$f(\vec{x}) = L(\vec{x}) + \gamma D_{\vec{u}}(\vec{x}), \tag{2}$$

where $L(\vec{x})$ is the log-likelihood function defined as:

$$L(\vec{x}) = \sum_{i=1}^{m} \left[b_i \exp(-\langle \vec{a_i}, \vec{x} \rangle) + y_i \langle \vec{a_i}, \vec{x} \rangle \right], \tag{3}$$

γ is a hyperparameter, $\vec{u} = (u_1, \ldots, u_n)$ is the reference image and $D_{\vec{u}}(\vec{x})$ is a distance function between the image $\vec{x}$ and the reference image $\vec{u}$ and is defined as:

$$D_{\vec{u}}(\vec{x}) = \sum_{j=1}^{n} d(x_j, u_j), \qquad d(a, b) = |a - b|. \tag{4}$$

The cost function in Eq. (2) is designed to search for the feasible solution that fit with the data using the log-likelihood function and at the same time close to the reference image in sense of ℓ_1 norm measurements.

The iterative reconstruction algorithm is derived using the majorization-minimization strategy [4], [6] and is summarized as:

1 Initialization $x^{(0)} = \epsilon$, with $\epsilon > 0$, $k \leftarrow 0$
repeat
  for $j = 1 : n$ **do**
2 $p_j = x_j^k + x_j^k \frac{\sum_i a_{ij}\left[b_i \exp(-\langle \vec{a_i}, \vec{x}^k \rangle) - y_i\right]}{\sum_i a_{ij} \langle \vec{a_i}, \vec{x}^k \rangle b_i \exp(-\langle \vec{a_i}, \vec{x}^k \rangle)}$
  $t_j = \gamma x_j^k / \sum_i a_{ij} \langle \vec{a_i}, \vec{x}^k \rangle b_i \exp(-\langle \vec{a_i}, \vec{x}^k \rangle)$
3 $x_j^{k+1} = Th(p_j, u_j, t_j)$
  end
  $k \leftarrow k + 1$
until *stopping criterion*;

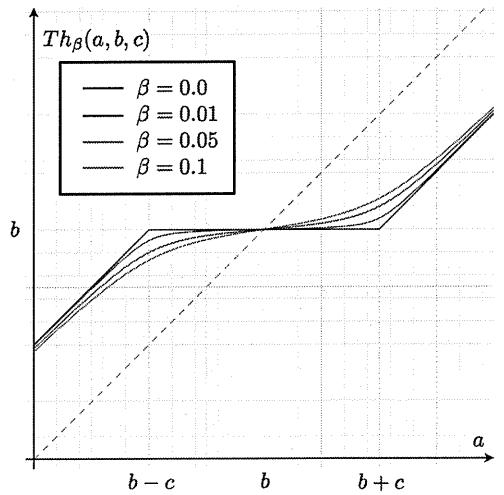

Fig. 1. Soft-thresholding function in Eq. (6) with different values of β.

where the thresholding function Th is defined as:

$$Th(a,b,c) = \begin{cases} a-c & (a > b+c) \\ a+c & (a < b-c) \\ b & (otherwise) \end{cases} . \quad (5)$$

In practical implementation, the soft-thresholding functions in Eq. (5), trims the pixel value p_j to the corresponding pixel value in the reference image u_j when it is relatively close. Otherwise, p_j is shifted *softly* towards the reference pixel intensity value [5].

B. Adaptive thresholding

The soft-thresholding function in Eq. (5) is non-convex. Due to this, incorrect thresholding may occur especially in pixels close to the boundaries. We generalize the soft-thresholding function by adding a convexity parameter β so that Eq. (5) is re-written as:

$$Th(a,b,c) = a + \frac{1}{2}\sqrt{(a-(b+c))^2+\beta} - \frac{1}{2}\sqrt{(a-(b-c))^2+\beta}, \quad (6)$$

where β is a small value that represents the convexity strength. When $\beta = 0$, Eqs. (5) and (6) become identicals as shown in Fig. 1.

C. Control priors uncertainty

One major drawback of practical implementation of reconstruction methods, that use a reference image similar to the one we propose here, is the consideration of the registration errors. Image shift or rotation of the registered reference image may reduce the image quality due to incorrect value of the corresponding reference pixel. In this regard, we propose a new global comparison strategy such that each image pixel x_j is associated to a corresponding window of a dynamic reference image instead of the comparison to a single pixel u_j in the reference image. The dynamic reference image is

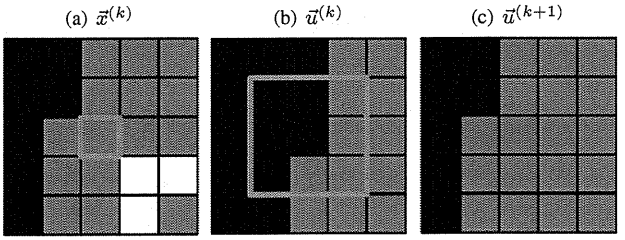

Fig. 2. Dynamic reference image, (a) is the current image estimate, (b) is the current reference image. The reference image for next iteration is computed using 3 × 3 window as in (c).

computed from the original reference and the current estimate of the reconstructed image such that:

$$u_j^{(k+1)} = \min_{u_i^{(k)}} \{d(x_j^{(k)}, u_i^{(k)})\}, i \in C \quad (7)$$

where C is a small window such as 3 × 3 pixels. In other words, each pixel of the reference image at the iteration $k+1$ is selected as one of the neighbor pixels in the reference image at iteration k, which is the closest to the corresponding pixel in the image estimate at iteration k. A simple example is shown in Fig. 2.

III. Experimental Results

We implemented a simulation study using the standard head Shepp-Logan phantom with image size 512×512 pixels and projection data measured using parallel-beam geometry using 512 (bins) and 32, 24, 20, and 16 projection angels over 180°. The reference image used is a simple uniform image shown in Fig. (3)(b). The proposed iterative reconstruction algorithm with the original thresholding function in Eq. (5) and the new one in Eq. (6) were implemented for 500 iterations. Reconstructed images and FBP reconstruction are shown in Fig. 3. The image reconstructed using the standard thresholding strategy looks smooth with significant reduction of streak artifacts. However, pixels located close to boundaries are not correctly restored with this relatively small number of iterations. However, by using the adaptive thresholding approximation with small $\beta = 0.001$, these drawbacks can be avoided.

In another study, we have used a star-shaped uniform reference image, shown in Fig (4)(a), such that a strong mismatch between the reconstructed image and the reference image is exist. We have used the dynamic reference approach given by Eq. (7) and the reference image is update side by side with the reconstructed image. We have used projection data measured over 32 projection views and a 3 × 3 window size. It is noticed from results, shown in Fig. 4, that as long as iteration proceeds, the dynamic reference images is corrected to the one that is used in Fig. 3(b).

IV. Conclusion

In this paper we discuss iterative reconstruction method that include *a priori* knowledge of reference image into account. In the framework of compressed sensing, the developed method take the form of two main steps. The first step is image update

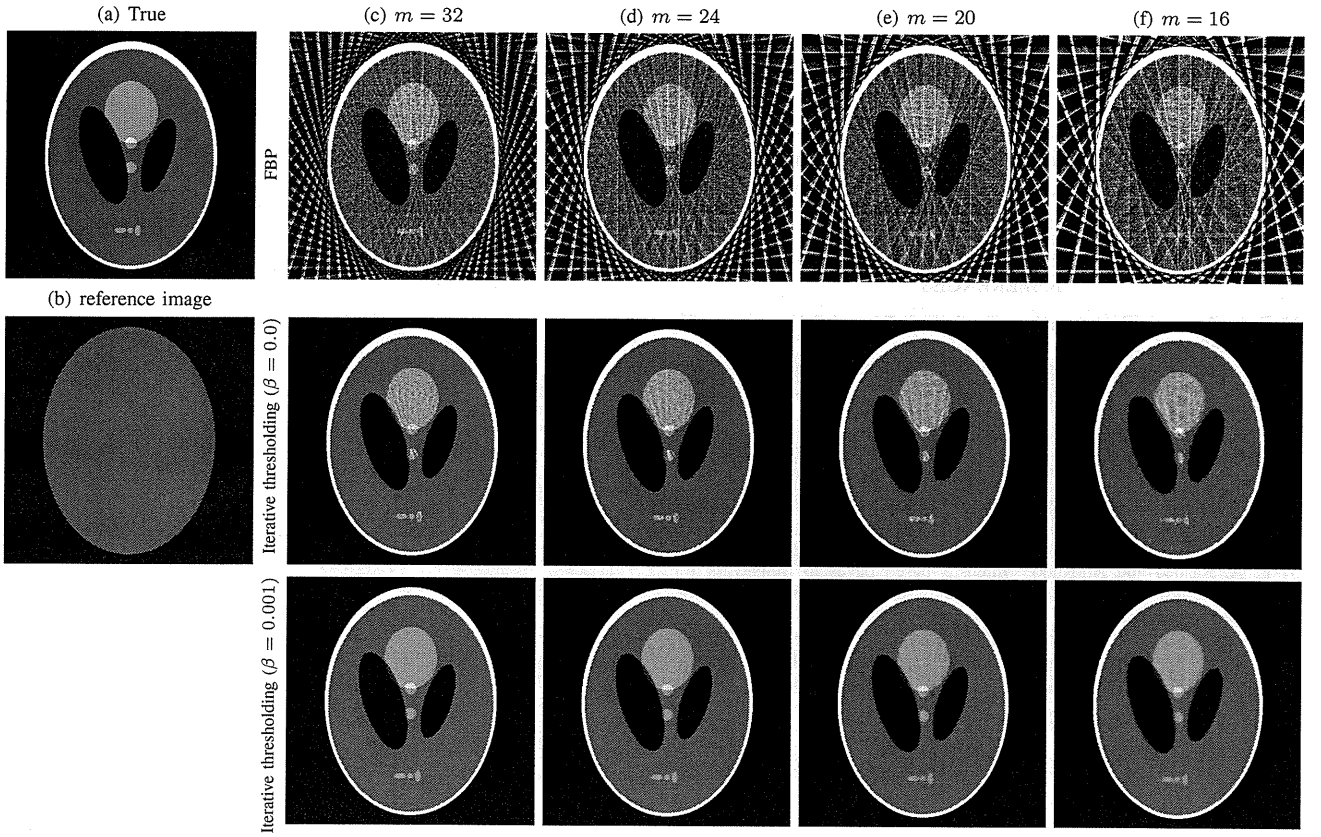

Fig. 3. Dynamic reference image, (a) is the current image estimate, (b) is the current reference image. The reference image for next iteration is computed using 3×3 window as in (c).

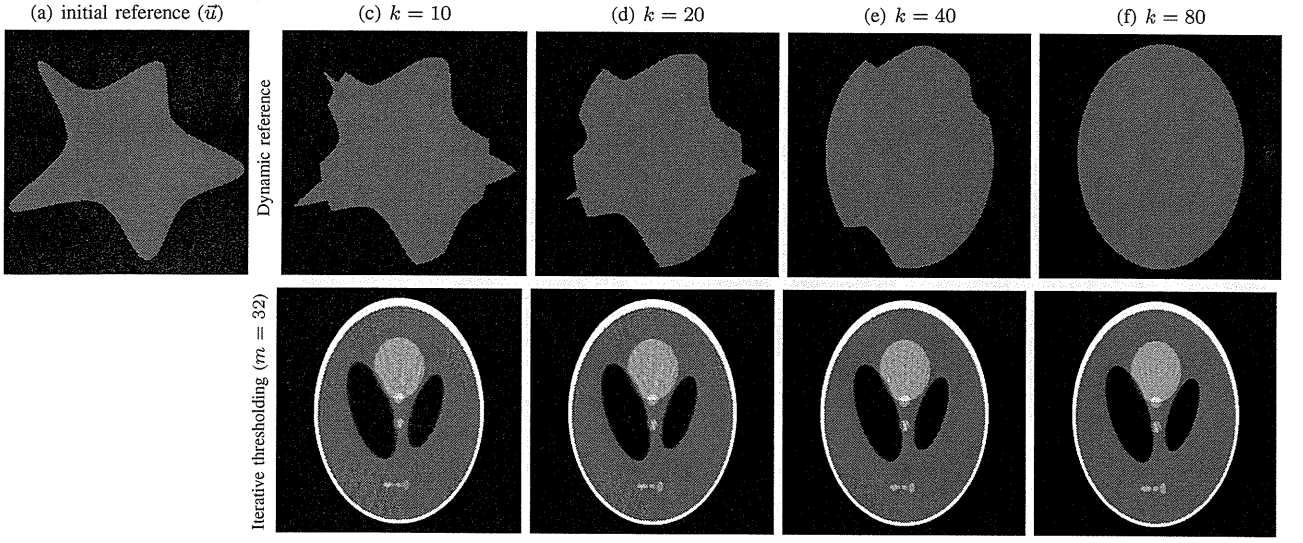

Fig. 4. Dynamic reference image, (a) is the current image estimate, (b) is the current reference image. The reference image for next iteration is computed using 3×3 window as in (c).

followed by a thresholding function. We develop adaptive thresholding function that can handle incorrect thresholding error. Moreover, we present a new approach toward control the misalignment between the reconstructed image and the *a priori* known reference image. The reference image is dynamically updated based on information from the current image estimate and the reference image in the previous iteration. Results presented in the paper is a preliminary results towards a full dynamic iterative image reconstruction protocol.

REFERENCES

[1] D. L. Donoho, "Compressed sensing," *IEEE Trans. Inf. Theory*, vol. 52, pp. 1289-1306, 2006.

[2] E. J. Candès, J. Romberg and T. Tao, "Robust uncertainty principles: exact signal reconstruction from highly incomplete frequency information," *IEEE Trans. Inf. Theory*, vol. 52, pp. 489-509, 2006.

[3] H. Yu and G. Wang, "A soft-threshold filtering approach for reconstruction from a limited number of projections," *Phys. Med. Biol.*, vol. 55, pp. 3905-3916, 2010.

[4] Y. Mameuda and H. Kudo, "New anatomical-prior-based image reconstruction method for PET/SPECT," *Conference Record of 2007 IEEE Medical Imaging Conference*, Paper No. M23-2, 2007.

[5] E. A. Rashed and H. Kudo, "Intensity-based bayesian framework for image reconstruction from sparse projection data," *Med. Imag. Tech.*, vol. 27, pp. 243-251, 2009.

[6] I. Daubechies, M. Defrise and C.De Mol, "An iterative thresholding algorithm for linear inverse problems with a sparsity constraint," *Comm. Pure Appl. Math.*, vol. 57, pp. 1413-1457, 2004.

Towards a High-Resolution Local Tomography Using Statistical Iterative Reconstruction

Essam A. Rashed, *Member, IEEE,* Hiroyuki Toda, Toshihiro Sera, Akira Tsuchiyama, Tsukasa Nakano, Kentaro Uesugi and Hiroyuki Kudo, *Member, IEEE*

***Abstract*—Synchrotron radiation (SR) x-ray micro-CT is an effective method for high-resolution imaging of small objects with several applications in biology and industry. However, the detector field of view is tiny, which limits the sample size to a few millimeters. When the sample size is larger than the limited field of view, reconstructed images, using conventional methods, known to suffer from DC-shift and low-frequency artifacts. This problem is known as local tomography or interior problem. In this paper we introduce a statistical iterative image reconstruction method to eliminate image artifacts produced from local tomography. The proposed method can be used in several SR imaging applications to enable a high resolution of the scanned object while preserving the image quality from artifacts produced due to the local tomography problem.**

I. Introduction

Synchrotron radiation (SR) micro-CT systems that provide a high-resolution cross-sectional images of small animals and other applications had a strong impact in several research fields such as drug developments. To obtain high-resolution CT images, it is required that the object is located completely inside the detector field of view (FOV). However, in many cases, a portion of the scanned object lies outside the FOV which leads to a truncation in the acquired projection data. Data truncation may also occur due to the magnification of a specific portion of the object or to reduce unnecessary radiation to the remaining portion of the object (Fig. 1). The most sever truncation case is when the projection data is truncated in all view angles providing the so-called local tomography or the interior problem [1]. It is known that when the projection data is fully truncated such as the case of local CT imaging, the reconstructed images suffers from DC-shift (or cupping) and low-frequency artifacts. These artifacts become strong in regions close to the boundaries of the FOV. The local tomography is also known as an ill-posed inverse problem which had been studied for a long time. Based on the analytical reconstruction, it was believed that all projection rays passing through the whole object are required for exact reconstruction and any truncation leads to losing the solution exactness. However, the recently developed theories based on the concept of Differentiated Backprojection (DBP) [2]–[4] and Backprojection-Filtration (BPF) [5] succeeded in reducing the required set of projection rays for theoretically exact and stable reconstruction.

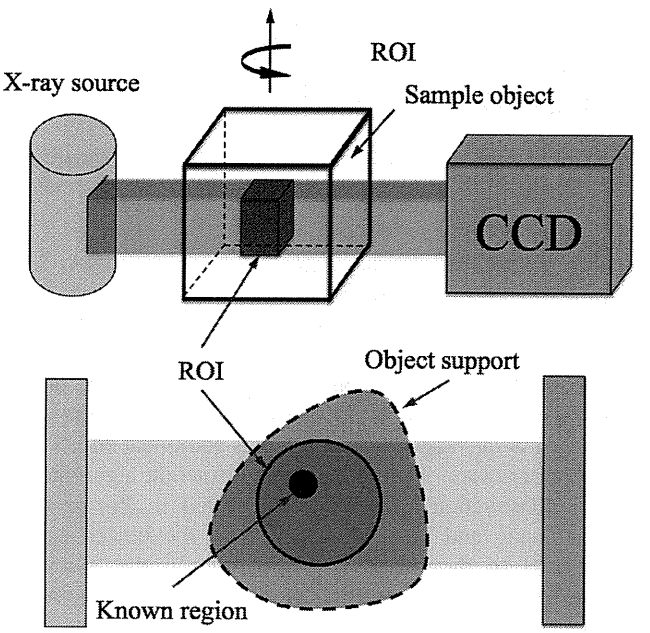

Fig. 1. Local tomography in SR micro-CT. The sample object usually extend outside the FOV of the CCD used for data acquisition. For accurate reconstruction, it required to know the object contour line (object support in additional to a region inside the region of interest (ROI).

In our earlier work, we proposed a statistical iterative reconstruction algorithm for region-of-interest (ROI) reconstruction when the projection data is partially truncated [6]. Here, we extend this algorithm to the case of local tomography. Experimental results using real data obtained from high-resolution SR imaging indicates a significant reduction in the image artifacts when the proposed method is used.

II. Proposed Method

A. Object support constraint

According to the theories based on the analytical concept of Hilbert transform in [3], [4], [7], it is possible to reconstruct exact image from locally truncated data if the following constrains are satisfied. 1) All projection rays passing through

This work was partially supported by Grant-in-Aid from the Japan Society for the Promotion of Science (JSPS). Grant for foreign post-doctoral fellows (ID No. P10052).

E.A.Rashed and H.Kudo are with the Department of Computer Science, Graduate School of Systems and Information Engineering, University of Tsukuba, Tsukuba 305-8573, Japan. H.Toda is with the Toyohashi University of Technology, Toyohashi, Japan, T.Sera and A.Tsuchiyama are with the Osaka University, Osaka, Japan. T.Nakano is with the AIST, Tsukuba, Japan. K.Uesugi is with the Japan Synchrotron Radiation Research Institute, Hyogo, Japan. E.A.Rashed is also with the Department of Mathematics, Faculty of Science, Suez Canal University, Ismailia 41522, Egypt (e-mail: essam@imagelab.cs.tsukuba.ac.jp).

978-1-4673-0119-0/11/$26.00 ©2011 IEEE

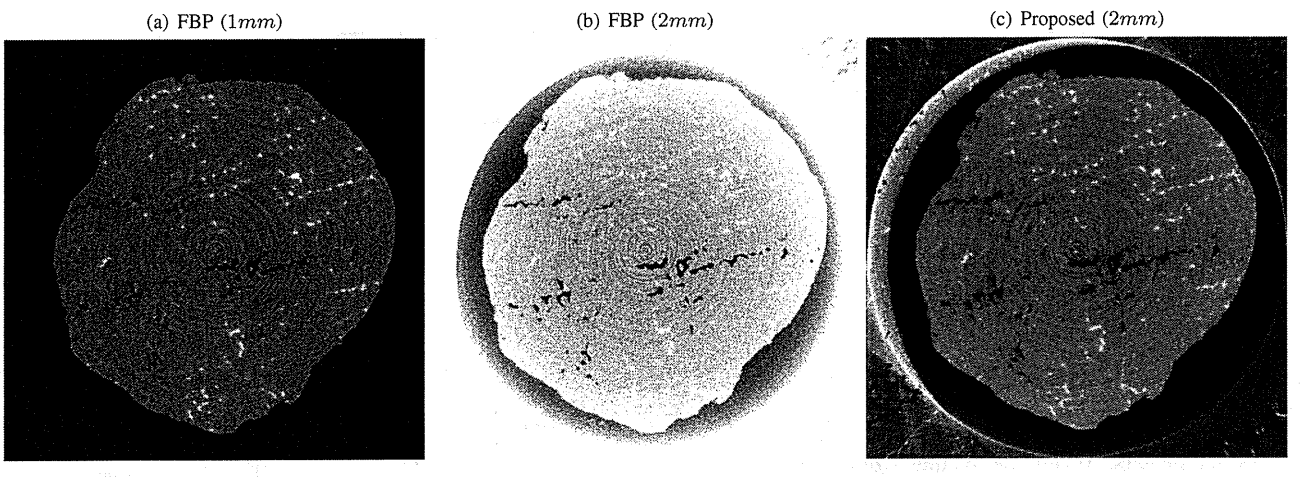

Fig. 2. Image reconstruction for the Aluminum alloy data. (a) Image reconstructed using FBP method from non-truncated data, to be used as true reference. Images reconstructed from local data using FBP algorithm in (b) and proposed method in (c).

FOV are included in the measured projection data, 2) a compact support of the object is available, 3) *a priori* known information of intensity value for small region inside the FOV is available, and 4) for iterative reconstruction, the image matrix should be large enough to include the entire object. The second constraint is not always available, as the exact definition of the object contour requires additional efforts such as extra hardware. The iterative reconstruction algorithm for ROI reconstruction (ROI-OSEM), detailed in [6], provides an automatic and efficient detection of the object support in parallel to the image reconstruction. In the following, we review the main approach of the ROI-OSEM algorithm with modifications that suits the correct noise modeling in transmission CT:

B. Iterative reconstruction algorithm

We consider the following noise model:

$$y_i \approx \text{Poisson } [b_i \exp(-\langle \vec{a_i}, \vec{x} \rangle)] \tag{1}$$

where $\vec{x} = (x_1, \ldots, x_n)^\top$ is the image vector, $\vec{y} = (y_1, \ldots, y_m)^\top$ be the measured counts, $\vec{b} = (b_1, \ldots, b_m)$ is the blank scan, $A = \{a_{ij}\}$ is the $m \times n$ system matrix and $\langle ., . \rangle$ is the regular inner product. The cost function for image reconstruction is defined as:

$$f(\vec{x}) = L(\vec{x}) + \beta T(\vec{x}), \tag{2}$$

where $L(\vec{x})$ is the negative log-likelihood function, $T(\vec{x})$ is a penalty function based on ℓ_0 norm and β is a hyperparameter defined as:

$$L(\vec{x}) = \sum_{i=1}^{m} \left[b_i \exp(-\langle \vec{a_i}, \vec{x} \rangle) + y_i \langle \vec{a_i}, \vec{x} \rangle \right], \tag{3}$$

$$T(\vec{x}) = \sum_{j=1}^{n} s(x_j), \quad s(t) = \lim_{\epsilon \to 0} |t|^\epsilon \equiv \begin{cases} 1 & t \neq 0 \\ 0 & t = 0 \end{cases}. \tag{4}$$

The formulation of the image reconstruction cost function in Eq. (2) can be simply indicate that, the reconstructed image is the most sparse image that fit with the measured projection data. This approach can successfully find the object support by threshold the image pixels that is close to zero to the value of zero. The minimization of cost function using the majorization-maximization approach [8] leads to the following iterative reconstruction algorithm:

1 Initialization $x^{(0)} = \epsilon$, with $\epsilon > 0$, $k \leftarrow 0$
repeat
  for $j = 1 : n$ **do**
2 $p_j = x_j^k + x_j^k \dfrac{\sum_i a_{ij} \left[b_i \exp(-\langle \vec{a_i}, \vec{x}^k \rangle) - y_i \right]}{\sum_i a_{ij} \langle \vec{a_i}, \vec{x}^k \rangle b_i \exp(-\langle \vec{a_i}, \vec{x}^k \rangle)}$
    $t_j = \dfrac{\sum_i a_{ij} \langle \vec{a_i}, \vec{x}^k \rangle b_i \exp(-\langle \vec{a_i}, \vec{x}^k \rangle)}{2\beta x_j^k}$
3 $x_j^{k+1} = \begin{cases} 0 & (p_j \leq \sqrt{1/t_j}) \\ p_j & (otherwise) \end{cases}$
  end
  $k \leftarrow k + 1$
until *stopping criterion*;

III. Experimental Results

In the experiment studies, we have used a three-dimensional high-resolution CT data obtained from a third-generation synchrotron radiation source located in Hyogo, Japan (SPring-8) [9].

A. Aluminum alloy data

In the first experiment, the object sample was a metallic Aluminum alloy (Al-Cu). In this imaging application, the air holes and the distribution of the alloy components are required to be observed in the sample. Two sets of data are used, the first one was acquired using sample of size $1mm$, which is completely fit inside the FOV to be used as a true reference for the later scan. The second dataset was acquired using a sample of size $2mm$ by including an external shield to the original sample imaged earlier. The data is acquired from BL20XU beamline with CCD of 2000×1312 that reconstructed in

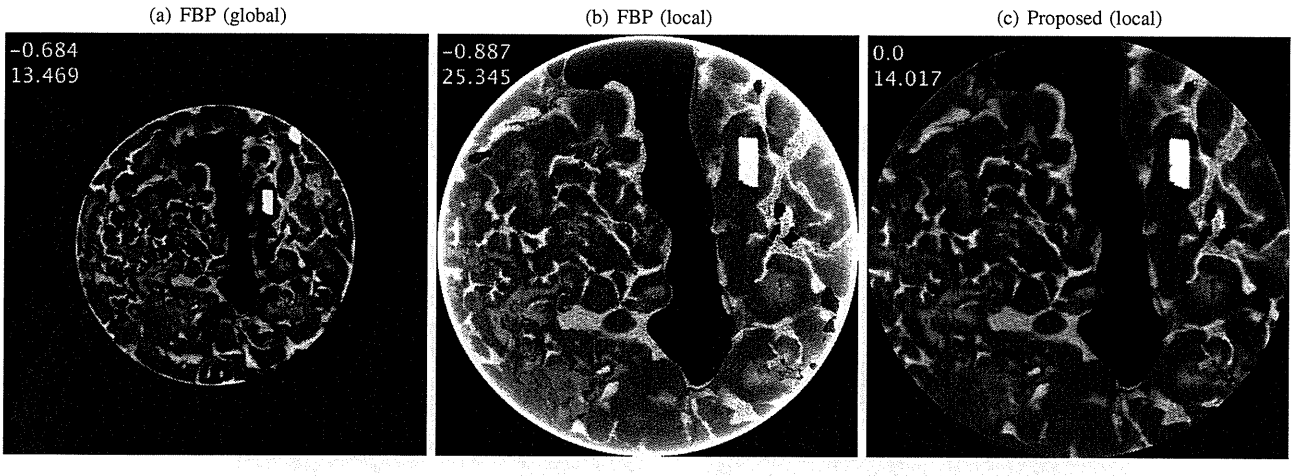

Fig. 3. Global image reconstructed from full projection data (left), local images reconstructed using standard FBP algorithm (middle), and ROI-OSEM algorithm (right). Intensity value ranges are displayed on top left corner of each images.

volume of size $2000 \times 2000 \times 1312$ with pixel size of $0.5\mu m$. The projection data was measured for 1500 views over 180° with energy of 35 keV. A single slice of the first dataset, which is not truncated, was reconstructed using FBP algorithm. The corresponding slice in the second dataset was reconstructed using FBP and proposed method. Results, shown in Fig. 2, indicate that the proposed method can reduce the DC-shift and low-frequency artifacts in the image reconstructed from local data.

B. Calcite in tarc

In this experiment, the object was a sample of tarc fluid containing calcite powder. In this application, it is required to investigate the internal structure of micro-size sample. The exact intensity value is important to identify the correct structure and any DC-shift occurs due to data truncation may lead to incorrect identification of the sample contents. Two sets of data, global and local, were acquired using an x-ray energy of 20 keV at BL20B2 beamline. The global data was obtained using a detector size of 1560×680 bins with bin size of 6.66 μm. In these settings the whole object was located completely inside the detector FOV and the projection data was computed over 2250 view angles over 180°. The local data was acquired with a magnification of the central region of the sample. The data was obtained using a detector of size 2000×1312 bins with bin size of 3.33 μm and 3000 view angels over 180°. Although, the local data provides a higher resolution (doubled) to the central region of the sample, the projection data was fully truncated and represents a local tomography.

The global data corresponding to central slice was used to reconstruct image of the whole object with 1560×1560 pixels using standard FBP algorithm, shown in Fig. 3(a) to be used as a reference for the evaluation of the proposed method. The local data of the central slice was used to reconstruct a magnified image of 2000×2000 pixels of an internal structure of the sample. The reconstruction using standard FBP and proposed method with 10 iterations are shown in Fig. 3. The proposed method succeeded in reducing the artifacts existing in the analytical reconstruction from local projection data. The correct estimation of the object support and the internal region, corresponding to air hole, lead to an exact local reconstruction.

C. Mouse lung

In this experiment, a real data acquired from a mouse, was used to investigate the structure of lung alveoli. The mouse was imaged BL20B2 beamline. The projection data was acquired using a detector of 2000×300 bins with bin size of 3.33 μm with a set of 1500 projection angles over 180°. The projection data was fully truncated such that the detector FOV was located completely inside the mouse. No information regarding the true object were measured during data acquisition. A single slice was reconstructed using standard FBP and the proposed method. The reconstructed images and the corresponding central horizontal and vertical profiles are shown in Fig. 4.

IV. Conclusion

In this work, we proposed statistical iterative reconstruction algorithm for local tomography. The proposed method is based on simple approach that effectively estimate the require *a priori* known information for accurate and stable reconstruction from fully truncated projection data. The proposed method is tested using SR micro-CT real data and effective achievement in image quality is observed compared to conventional methods. However, the computation cost of the proposed method still the major challenge. Future work include the reducing the computation cost to a reasonable level for practical implementation in high-resolution micro-CT imaging.

References

[1] F. Natterer, *The Mathematics of Computerized Tomography*, Philadelphia, PA: Wiley, 1986.

[2] F. Noo, R. Clackdoyle and J. D. Pack, "A two-step Hilbert transform method for 2D image reconstruction," *Phys. Med. Biol.*, vol. 49, pp. 3903-3923, 2004.

[3] M. Defrise, F. Noo, R. Clackdoyle and H. Kudo, "Truncated Hilbert transform and image reconstruction from limited tomographic data," *Inverse Problems*, vol. 22, pp. 1037-1053, 2006.

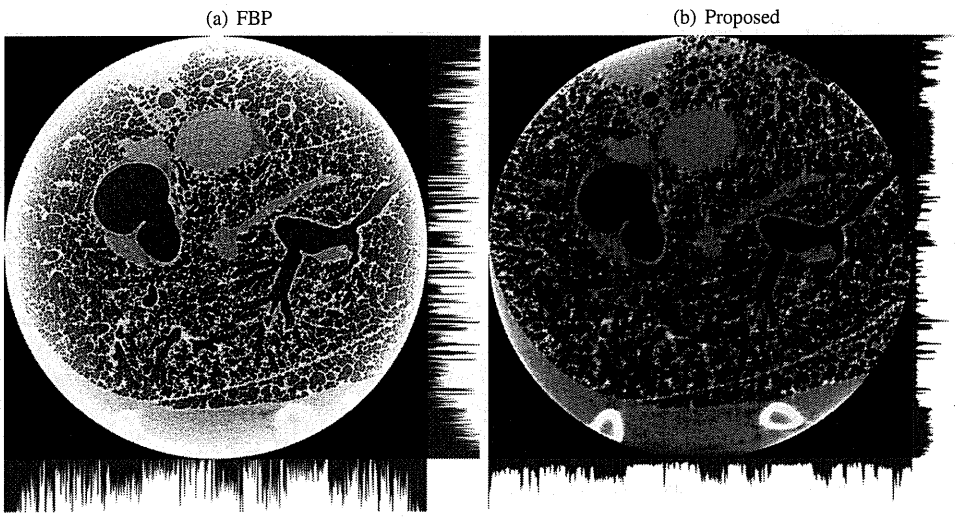

Fig. 4. Reconstructed images using FBP algorithm (left) with strong DC-shift and low-frequency artifacts and using the proposed iterative method (right) show a significant artifact reduction. Central horizontal and vertical profiles are also shown.

[4] H. Kudo, M.Courdurier, F.Noo and M.Defrise, "Tiny *a priori* knowledge solves the interior problem in computed tomography," *Phys. Med. Biol.*, vol. 53, pp. 2207-2231, 2008.
[5] X. Pan, Y. Zou and D. Xia, "Image reconstruction in peripheral and central regions-of-interest and data redundancy," *Med. Phys.*, vol. 32, pp. 673-684, 2005.
[6] E. Rashed and H. Kudo, "Region-of-Interest reconstruction from truncated projection data under blind object support", *Conference Record of 2008 IEEE Medical Imaging Conference*, Paper No. M03-7, 2008.
[7] Y. Ye, H. Yu, Y. Wei and G. Wang, "A general local reconstruction approach based on a truncated Hilbert transform," *Int. J. Biomed. Imaging*, vol. 2007, Article ID 63634 (8 pp), 2007.
[8] J. A. Fessler and A. O. Hero, "Penalized maximum-likelihood image reconstruction using space-alternating generalized EM algorithms," *IEEE Trans. Image Process.*, vol.4, pp. 1417-1429, 1995.
[9] http://www.spring8.or.jp

Iterative Thresholding Framework for Row-Action Reconstruction from Sparse Projection Data

Essam A. Rashed, *Member, IEEE,* and Hiroyuki Kudo, *Member, IEEE*

***Abstract*—This paper presents a framework for row-action type iterative reconstruction from projection data measured over small number of projection views, or sparse projections. Image reconstruction from sparse projections usually suffers from streak artifacts that degrade the image quality. However, this imaging scenario becomes a hot topic of research due its possibilities to reduce patient dose and other benefits in several imaging applications. The motivation behind this work is the use of ℓ_1/ℓ_0 norm distance to a reference image to select the sparse solution corresponding to the difference between the reconstructed image and the reference image. The concept of Lagrangian duality is used to derive the iterative thresholding framework which can be classified as an ART-like reconstruction method. The work presented here can be thought as a generalization of the previous work in (Li et al., 2004) which mainly focuses on the reconstruction of sparse objects, such as blood vessels. However, most of clinical applications consider imaging of non-sparse objects. The extension to the general case of x-ray computed tomography (CT) imaging, where the target object is non-sparse, is presented here. Experimental data indicates the power of the proposed method in reducing streak artifacts produced from data down-sampling.**

I. Introduction

This paper presents a framework for row-action type iterative reconstruction from projection data measured over small number of projection views, or sparse projections. Image reconstruction from sparse projections usually suffers from streak artifacts that degrade the image quality. However, this imaging scenario becomes a hot topic of research due its possibilities to reduce patient dose and other benefits in several imaging applications [1]–[4]. The motivation behind this work is the use of ℓ_1/ℓ_0 norm distance to a reference image to select the sparse solution corresponding to the difference between the reconstructed image and the reference image. The concept of Lagrangian duality is used to derive the iterative thresholding framework which can be classified as an ART-like reconstruction method. The work presented here can be thought as a generalization of the previous work in [5] which mainly focuses on the reconstruction of sparse objects such as blood vessels. However, most of clinical applications consider imaging of non-sparse objects. The extension to the general case of x-ray computed tomography (CT) imaging, where the target object is non-sparse, is presented here.

This work was partially supported by Grant-in-Aid from the Japan Society for the Promotion of Science (JSPS). Grant for foreign post-doctoral fellows (ID No. P10052).

E.A.Rashed and H.Kudo are with the Department of Computer Science, Graduate School of Systems and Information Engineering, University of Tsukuba, Tsukuba 305-8573, Japan. E.A.Rashed is also with the Department of Mathematics, Faculty of Science, Suez Canal University, Ismailia 41522, Egypt (e-mail: essam@imagelab.cs.tsukuba.ac.jp).

II. Proposed Method

A. Problem formulation

In earlier work [5], the sparse solution to the linear constraint is picked up using the linear program:

$$\text{minimize } \|\vec{x}\|_1 \text{ subject to } \vec{x} \geq 0, A\vec{x} = \vec{y}, \tag{1}$$

where $\vec{x} = (x_1, \ldots, x_n)^\top$ is the image vector, $\vec{y} = (y_1, \ldots, y_m)^\top$ is the projection data and $A = \{a_{ij}\}$ is the system matrix. This cost function was formulated with consideration that $\vec{x}$ is sparse (i.e. the object to be imaged has only a small number of non-zero pixels). The motivation here is how to implement this method in general x-ray CT imaging, where the object is usually non-sparse. The formulation of sparse object is possible if some *a priori* information, such as a reference image, is available. The abnormalities, such as lesions and cancer indicators, usually appear in small regions of the imaged object. Therefore, subtracting the normal structures known in prior to the reconstruction is expected to result in a sparse image domain that includes unexpected or abnormal structures. This assumption holds if the registration error between the reference image and the reconstructed image is small. The proposed linear program to be considered here is as follows:

$$\text{minimize } \|\vec{x} - \vec{u}\|_1 \text{ s.t. } \vec{x} \geq 0, A\vec{x} = \vec{y}, \tag{2}$$

where $\vec{u} = (u_1, \ldots, u_n)^\top$ is a reference image to $\vec{x}$. The minimization of (2) is applied by computing the corresponding dual problem using Lagrangian duality. The maximization of the dual problem corresponds to the minimization of the original problem [6]. To approximate the solution, the linear program in Eq. (2) is perturbed to get the following quadratic program:

$$\text{minimize } \sum_{j=1}^{n} \left(\frac{\epsilon}{2}(x_j - u_j)^2 + |x_j - u_j| \right) \text{ s.t. } A\vec{x} = \vec{y}, \vec{x} \geq 0, \tag{3}$$

where ϵ is a small positive number. Similar to the implementation in [5], Eq. (3) is re-written as follows:

$$\text{minimize } F_{\vec{u}}(\vec{x}) \text{ s.t. } A\vec{x} = \vec{y}, \tag{4}$$

$$F_{\vec{u}}(\vec{x}) = \sum_{j=1}^{n} f_{u_j}(x_j), \quad f_a(t) = \frac{\epsilon}{2}(t-a)^2 + |t-a|.$$

978-1-4673-0119-0/11/$26.00 ©2011 IEEE

The Lagrangian dual problem of (4) is the following unconstrained maximization problem:

$$\text{maximize } D(\vec{\lambda}) = \vec{y}^{\top}\vec{\lambda} - G_{\vec{u}}(A^{\top}\vec{\lambda}), \tag{5}$$

where $\vec{\lambda} = (\lambda_1, \ldots, \lambda_m)^{\top}$ is a real vector and $G_{\vec{u}}(.)$ is known as the conjugate function and is defined as:

$$G_{\vec{u}}(\vec{b}) = \sum_{i=1}^{n} g_{u_j}(b_j), \tag{6}$$

$$g_a(t) = \begin{cases} -\frac{1}{2}\epsilon a^2 - a & (t < -1 - \epsilon a) \\ at + \frac{(t+1)^2}{2\epsilon} & (-1 - \epsilon a \le t < -1) \\ at & (-1 \le t < 1) \\ at + \frac{(t-1)^2}{2\epsilon} & (t \ge 1) \end{cases}. \tag{7}$$

Assuming that $\vec{x}^*$ and $\vec{\lambda}^*$ are the optimal solutions for (4) and (5), respectively, then $\vec{x}^*$ can be computed from $\vec{\lambda}^*$ with the primal-dual relation defined as:

$$x_j^* = g'_{u_j}\left(A^{\top}\vec{\lambda}^*|_j\right), \tag{8}$$

$$g'_a(t) = \begin{cases} 0 & (t < -1 - \epsilon a) \\ a + \frac{t+1}{\epsilon} & (t < -1) \\ a & (-1 \le t < 1) \\ a + \frac{t-1}{\epsilon} & (t \ge 1) \end{cases}. \tag{9}$$

B. Iterative reconstruction framework

The solution of the maximization problem in (6) is done by the Newton-like coordinate ascent method. The final form of the iteration is summarized as follows:

1 Compute reference image $\vec{u} = (u_1, \ldots, u_n)$
2 Initialization $w^{(0)} = (0, \ldots, 0)$, $k \leftarrow 0$
3 **repeat**
  $\vec{w}^{(k,1)} = \vec{w}^{(k)}$
  for $i = 1 : m$ **do**
    $\vec{w}^{(k,i+1)} = \vec{w}^{(k,i)} + \frac{y_i - \sum_{j=1}^{n} a_{ij} g'_{u_j}(w_j^{(k,i)})}{\frac{1}{\epsilon}\sum_{j=1}^{n} a_{ij}^2}\vec{a_i}$
  end
  $\vec{w}^{(k+1)} = \vec{w}^{(k,m+1)}$
  $k \leftarrow k + 1$
until *stopping criterion*;
4 **for** $j = 1 : n$ **do**
  $x_j^* = g'_{u_j}(w_j^{(k+1)})$
end

The same approach can be implemented using ℓ_0 norm distance to formulate the cost function:

$$\text{minimize } \|\vec{x} - \vec{u}\|_0 \text{ s.t. } \vec{x} \ge 0, A\vec{x} = \vec{y}. \tag{10}$$

In this case, Eq. (7) can be derived as follows:

$$g_a(t) = \begin{cases} c & (t < t_c(a,\epsilon)) \\ at & (t_c(a,\epsilon) \le t < \sqrt{2\epsilon}) \\ \frac{t^2}{2\epsilon} + at - 1 & (t \ge \sqrt{2\epsilon}) \end{cases} \tag{11}$$

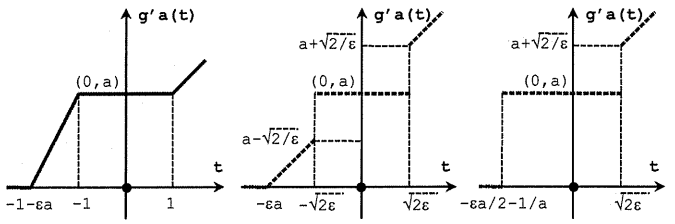

Fig. 1. Illustration of thresholding functions corresponding to Eq.(9) (left) and Eq.(13) with $a > \sqrt{2/\epsilon}$ (middle) and $a \le \sqrt{2/\epsilon}$ (right).

while $c = \min(\frac{t^2}{2\epsilon} + at - 1, -\frac{1}{2}\epsilon a^2 - 1)$ and

$$t_c(a,\epsilon) = \begin{cases} -\sqrt{2\epsilon} & (a > \sqrt{2/\epsilon}) \\ -\frac{1}{2}\epsilon a - \frac{1}{a} & (a \le \sqrt{2/\epsilon}) \end{cases}, \tag{12}$$

and the corresponding thresholding function, shown in Fig. 1, is given by:

$$g'_a(t) = \begin{cases} \max(a + \frac{t}{\epsilon}, 0) & (t < t_c(a,\epsilon)) \\ \max(a - \frac{1}{\sqrt{2\epsilon}}, \frac{a}{2}) & (t = t_c(a,\epsilon)) \\ a & (t_c(a,\epsilon) < t < \sqrt{2\epsilon}) \\ a + \frac{1}{\sqrt{2\epsilon}} & (t = \sqrt{2\epsilon}) \\ a + \frac{t}{\epsilon} & (t > \sqrt{2\epsilon}) \end{cases}. \tag{13}$$

The thresholding functions in Eqs. (9) and (13), shown in Fig. 1, have a close form to the soft/hard-thresholding operations used for image denoise in image processing literature. Unlike the case of ℓ_1 norm, the convergence of the ℓ_0 norm-based method is not assured.

III. Experimental Results

A simulation study was performed using a modified version of the Shepp-Logan phantom (Fig. 2). This study aims to observe the inserted spots with different reconstruction methods from small number of projection views. The image size was 512×512 pixels that is projected using 512(bins)×16(views) over 180° using parallel-beam geometry. The reference image $\vec{u}$ is assumed to be a uniform image shown in Fig. 2(b). The simulation is performed using 50 and 100 iterations using the ℓ_1, ℓ_0 norm-based methods, respectively. Reconstructed images are shown in Fig. 2.

IV. Conclusion

We presented iterative image reconstruction algorithm from small number of projection views. The main approach is based on minimizing the ℓ_1/ℓ_0 norm distance to *a priori* known reference image. Obviously, the accuracy of the reference image $\vec{u}$ has a strong contribution to the quality of the reconstructed image $\vec{x}$. However, we have found that a rough estimate, that could be obtained easily in several imaging application, is enough to eliminate streak artifacts significantly. The proposed row-action framework is simple, fast and easy to be implement to suit several imaging applications.